

Pyrolysis Kinetics of a Lignin-Modified Cellulose Composite Film

Ruohan Yang, Xinyu Lu,* and Xiaoli Gu*

Cite This: *ACS Omega* 2021, 6, 35584–35592

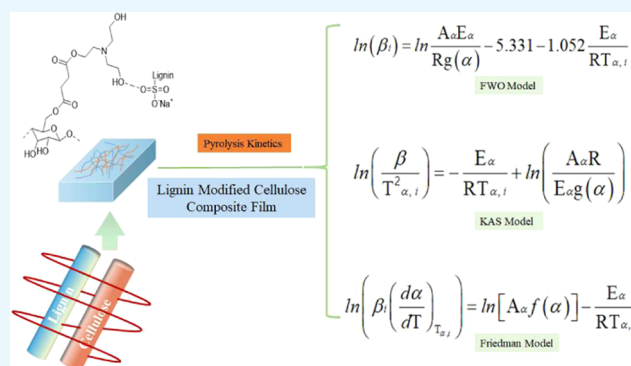
Read Online

ACCESS |

Metrics & More

Article Recommendations

ABSTRACT: Cellulose is the most abundant natural biopolymer material, which has been widely used in film making and food packaging in recent years. However, lignin, a natural bioaromatic material, is always applied as a waste resource due to its low utilization efficiency. In this study, a $\text{ZnCl}_2/\text{CaCl}_2$ /cellulose mixed system was used to prepare film materials via a regeneration method. The chemical structure and corresponding properties were characterized. The thermal decomposition process of film materials showed that with an increase of the heating rate, the maximum weight loss temperature gradually shifted to the higher-temperature region. Additionally, the combination of lignin with cellulose as composite films can effectively improve thermal stability. Furthermore, kinetics methods such as Kissing–Akahira–Sunose (KAS), Flynn–Wall–Ozawa (FWO), and Friedman were used to calculate the average activation energy (E). This study proposed a facile method for preparing biobased multifunctional composite films using two kinds of naturally renewable materials.



1. INTRODUCTION

Natural polymer materials, such as cellulose (or its derivatives), starch (or its derivatives), protein, chitin, etc., are sustainable and renewable.¹ Cellulose film has good biocompatibility, flexibility, chemical modification, and generality and promising applications in wastewater treatment, wound healing, packaging, and bacteriostasis.^{2–7}

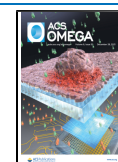
A transparent multifunctional cellulose platform membrane was prepared from eucalyptus pulp. The cellulose platform introduced multifunctional spiropropan group into cellulose molecule using a nucleophilic postmodification strategy, and the obtained multifunctional cellulose films had improved performance of UV shielding, photochromism, and mechanical solid strength.^{8,9} In the present work,¹⁰ the prepared bacterial cellulose film used bacterial cellulose as a substrate. The extra addition of nanocrystalline increased the tensile strength to 46.5 MPa and elongation at break to 13.5% and reduced the water vapor permeability to 17% to improve water resistance.¹¹ We prepared cellulose nanofiber (CNF), carboxymethyl cellulose nanofiber (CNFCM), enzyme-treated cellulose nanofiber (CNFENZ), TEMPO-oxidized cellulose nanofiber (CNFTEMPO), and sodium carboxymethyl cellulose nanofiber (CMC) films by the solution casting method. Results showed that the CNFENZ film had higher thermal stability and better water vapor resistance as compared to other samples. Furthermore, the better mechanism property was derived from the addition of carboxylic acid and carboxymethyl groups in CNFTEMPO and CNFCM films.

Lignin is the largest renewable bioaromatic material on earth. However, its low utilization efficiency has led to a large amount of waste.¹² Lignin can be mixed with cellulose to prepare lignin–cellulose mixed films to improve their mechanism, thermal stability, and oxidation abilities. Sodium lignosulfonate can be extracted from pulp and papermaking waste or from lignin sulfonation. Efficient utilization of lignin is beneficial to protecting our environment and reducing resource waste.¹³ Wu et al.¹⁴ used ionic liquid (IL)-1-allyl-3-methylimidazolium chloride (AmimCl) as solutions and cellulose, starch, and lignin as raw materials to prepare biobased composite films. Results showed that different contents of cellulose, lignin, and starch have a significant effect on mechanical, thermal, and water resistance. Besides, Zhang et al.¹⁵ prepared lignin–cellulose mixed nanofibers (LCNFs) from unbleached bark and used it as a reinforcing agent for thermoplastic starch (TPS) to obtain a novel biodegradable composite film. Results showed that LCNF had higher lignin content, and multiple functional groups of lignin can improve water resistance and thermal stability. Michelin et al.¹⁶ added organic soluble lignin as a reinforcing agent and a bioactive agent into CMC substrate to prepare composite films with compatible and environmentally friendly

Received: September 23, 2021

Accepted: December 7, 2021

Published: December 16, 2021



solvent. The addition of lignin improves water resistance and thermal stability.

In this study, cellulose was used as raw material to prepare cellulose films via the regeneration method using a $\text{ZnCl}_2/\text{CaCl}_2$ /cellulose mixed system. The cross-linking mechanism was proposed, and a lignin–cellulose composite membrane was obtained by adding sodium lignosulfonate with modification to change its mechanical, hydrophobic, and particularly thermal stability performance. Furthermore, three different kinetic methods were applied to calculate the activation energy during the film thermal decomposition process.

2. EXPERIMENT

2.1. Materials. In this study, α -cellulose with a particle size of 250 μm was purchased from Aladdin (Shanghai, China). Sodium lignosulfonate (SLS, 96%, with total sulfur of 5.2%, M_w of 3802 g/mol, and a phenolic hydroxyl content of 2.8 mmol/g SLS from nonaqueous phase potentiometric titration) was purchased from TCI (Shanghai, China). Other chemical reagents, such as zinc chloride (ZnCl_2 , 99%), calcium chloride (CaCl_2 , 99.9%), absolute ethanol (99.5%), succinic anhydride (98%), triethanolamine (98%), anhydrous calcium sulfate (CaSO_4 , 97%), and sodium carbonate anhydrous (Na_2CO_3 , 99.5%), were purchased from Macklin (Shanghai, China). All chemical reagents were used without any pretreatment, and deionized water was produced from our laboratory.

2.2. Experimental Section. **2.2.1. Film Preparation.** Briefly, 0.45 g of α -cellulose was added to 1.05 g of deionized water under continuous stirring for 30 min to obtain a cellulose suspension solution (recorded as solution I). Next, 9.87 g of ZnCl_2 was mixed with 0.30 g of CaCl_2 in 3.63 g of deionized water under stirring for 30 min; then, different amounts of SLS (10, 20, 30, and 40 wt %, based on cellulose input) were added to the ionic solution and stirred at 75 $^\circ\text{C}$ for 30 min (recorded as solution II). Solution II was dropped into solution I and further stirred at room temperature for 12 h. Finally, the obtained solution was placed in a vacuum atmosphere to remove air bubbles and cast on a glass plate to prepare a film with a thickness of 450 μm . Then, the film was soaked with 450 mL of anhydrous ethanol for 1 h. After separating the film from the glass plate, it was fixed with two splints immediately and dried overnight at room temperature. To facilitate the next experiment, the film was cut into a 2 cm \times 2 cm size, denoted as $\text{SLS}_X\text{-CF}$, where X represents the addition of SLS (wt %). For example, $\text{SLS}_0\text{-CF}$ means a pure cellulose film (CF) without SLS addition, while $\text{SLS}_{10}\text{-CF}$ is a mixed film sample with 10 wt % lignin incorporation.

2.2.2. Film Modification. Due to the presence of hydroxyl groups (O–H) in the structure of cellulose and lignin, it is possible to form a lignin–cellulose composite by cross-linking.^{17–19} It is hard to achieve direct intramolecular cross-linking via chemical modification. Therefore, effective “bridge linkages” formed by intramolecular condensation (i.e., succinic anhydride and triethanolamine) were introduced to improve their interaction. In general, polymerization esters can be formed between carboxylic acids and alcohols at certain temperatures. Theoretically, the combination of cellulose and lignin can be realized through the above mechanism.

First, succinic anhydride (0.18 g), triethanolamine (0.45 g), and anhydrous ethanol (100, 200, and 300 mL) were mixed to prepare different organic precursor solutions. Then, the pure CF ($\text{SLS}_0\text{-CF}$) was soaked with different organic precursor solutions for different times (1, 2, and 3 days). Finally, the soaked film was

cured at different temperatures (50, 60, 70 $^\circ\text{C}$) to complete chemical modification, then dried at curing temperatures for 12 h, and denoted as CF-M. The mechanical properties of the films were preliminarily evaluated to optimize the reaction conditions. Other mixed films containing different amounts of SLS were prepared under optimized conditions (30 mL of ethanol, 70 $^\circ\text{C}$, and 1 day of immersion) and denoted as $\text{SLS}_X\text{-CF-M}$.

2.3. Characterization Methods. The film thickness was measured using an ID-C112XBS micrometer (Mitutoyo Corp., Tokyo, Japan), and it presented an average value of five points. Fourier transform infrared (FTIR) spectroscopy was performed on a VERTEX 70 spectrometer. The range of measured wavenumbers was between 500 and 4000 cm^{-1} , and 32 scans per spectrum were collected with a resolution of 4 wavenumbers. The surface morphology was recorded using an S-4800 cold field emission scanning electron microscope (SEM). The thermal stability of prepared films was studied on a TA Instruments thermogravimetric analyzer (TGA) Q500 (TA Instruments) with a fixed heating rate of 10 $^\circ\text{C}/\text{min}$ from room temperature to 600 $^\circ\text{C}$ with a nitrogen flow of 40 mL/min. A tensile test was performed on the film with a strain rate of 30 mm/min at 25 $^\circ\text{C}$ via an auto tensile tester (SANS CMT4000). The medical film samples had a width and length of 10 and 35 mm, respectively. A Kruss DSA100 was used to obtain the water contact angle. Light transmission was carried out through the film (2 cm \times 2 cm) on a Lambda 950 UV–vis light-color meter in the wavelength range of 200–600 nm .

Water absorption:

$$\text{water absorption} = \frac{W_t - W_0}{W_t} \times 100\% \quad (1)$$

where W_t is the film mass measured at room temperature with different soaking times.

Cross-linking degree (CD %):

The degree of cross-linking (CD %) was measured by weighing the film soaked in chloroform for 24 h, and the following formula can be used to calculate the cross-linking degree

$$\text{CD}\% = \frac{W_{\text{initial}}}{W_{\text{soaked}}} \times 100\% \quad (2)$$

where CD % is the cross-linking degree, W_{initial} is the dry mass of the film, and W_{soaked} is the dry mass of the film after being soaked in chloroform, followed by extraction in a Soxhlet device.

Water vapor permeability (WVP): water vapor permeability was tested using ASTM standard method E96. A diameter of 2.7 cm was selected, and a typical bottle of volume 20 mL was used to measure the WVP of the film. First, the film was cut into a circle with a diameter of 2.8 cm (slightly larger than the mouth of the bottle used). Then, a certain amount of anhydrous CaSO_4 (moisture content = 0%) was added into 2/3 of the volume (about 3 g) and covered with different films. Each bottle was filled with a dryer (100 mL beaker) with a saturated Na_2CO_3 solution at the bottom. In addition, excess Na_2CO_3 was added to ensure saturation of the Na_2CO_3 solution, providing a constant relative humidity (RH) of 92% at 25 $^\circ\text{C}$. Each bottle was weighed 12 h and the mass changes were recorded. The slope of the line was obtained (mass change versus time) by linear regression. WVP is determined as the slope of the line divided by the transfer area ($\text{g}/(\text{days m}^2)$). All data measured was repeated in parallel and recorded three times.

2.4. Kinetic Modeling. **2.4.1. Dynamic Model.** Non-isothermal gravimetric analysis (TGA) is the most common method of dynamic analysis. Kinetic parameters were obtained by recording the mass loss versus time and determined by kinetic methods (inversion model fitting or its equivalent).^{20,21} The International Federation of Thermal Analysis and Calorimetry Dynamics Committee (ICTAC) does not recommend the former because of the inherent uncertainty in determining kinetic parameters.²² Isotropic inversion methods can be divided into two categories: integral and differential methods.²³ Among them, the most popular integration methods are Flynn–Wall–Ozawa (FWO) and Kissinger–Akahira–Sunose (KAS).^{24–28} In addition, because of its accuracy, Friedman (a differential method) is considered to be the most popular method among different methods. The specific formula is as follows

$$\frac{d\alpha}{dt} = K(T)f(\alpha) \quad (3)$$

$$\alpha = 1 - \frac{m_{(t)} - m_f}{m_0 - m_f} \quad (4)$$

As can be seen from eq 3, $f(\alpha)$ is the differential mechanism function, T is the temperature in Kelvin, the conversion rate α is defined as eq 4, m_0 represents the initial mass, $m_{(t)}$ represents the mass m at time t , and m_f represents the final mass.

$$k = A \times \exp\left(-\frac{E}{RT}\right) \quad (5)$$

In eq 5, A is the frequency factor (min^{-1}), E is the activation energy (kJ/mol), R represents the gas constant (8.314 J/(K mol)), and T indicates the temperature (K).

Equations 3 and 5 were combined to obtain eq 6 for calculating the kinetic parameters. The formula is as follows

$$\frac{d\alpha}{dt} = A \times f(\alpha) \times \exp\left(-\frac{E}{RT}\right) \quad (6)$$

where $f(\alpha)$ and its derivative $f'(\alpha) = -1$ are used to represent the first-order solid-state reaction. $f(\alpha)$ could be expressed as eq 7

$$f(\alpha) = (1 - \alpha)^n \quad (7)$$

where n indicates the number of reaction stages.

Equation 7 was substituted into eq 6 to obtain eq 8 of the reaction rate.

$$\frac{d\alpha}{dt} = A \times \exp\left(-\frac{E}{RT}\right)(1 - \alpha)^n \quad (8)$$

The heating rate β was defined as dT/dt . Substituting it into eq 8, we obtain eq 9.

$$\frac{d\alpha}{dt} = \frac{A}{\beta} \exp\left(-\frac{E}{RT}\right)(1 - \alpha)^n \quad (9)$$

The proportion of materials consumed at the time is represented as eq 9. According to eq 9, kinetic parameters of A , E , and n were obtained from the thermogravimetric experiment adopting various kinetic methods.

Under nonisothermal conditions with a constant heating rate, eq 3 can be written as

$$\frac{d\alpha}{dt} = \frac{A}{\beta} e^{-E/(RT)} f(\alpha) \quad (10)$$

where β is the heating rate (K/s), $\beta = \frac{dT}{dt}$.

According to different reports in the literature, three isoconversional methods can be expressed as given below.

2.4.2. Flynn–Wall–Ozawa (FWO) Method. The FWO model was expressed as eq 11. Five heating rates (10, 20, 30, 40, and 50 °C/min) were used to calculate the apparent activation energy (E_a), which is a function of the conversion rate (α). E_a can also be obtained from a linear graph of the logarithm (β), and $1000/T_{\alpha,i}$ is based on each conversion rate (α), where the slope is $-1.052 E_a/R$.

$$\ln(\beta_i) = \ln \frac{A_\alpha E_\alpha}{Rg(\alpha)} - 5.331 - 1.052 \frac{E_\alpha}{RT_{\alpha,i}} \quad (11)$$

In this formula, $g(\alpha)$ represents a specific conversion of a constant. Subscripts i and α refer to the heating rate of a given value (β) and conversion (α), respectively.

2.4.3. Kissinger–Akahira–Sunose (KAS) Method. The apparent activation energy (E_a) was also obtained at five heating rates of 10, 20, 30, 40, and 50 °C/min. The expression of KAS could be written as eq 12. In the formula, $T_{\alpha,i}$ represents the temperature corresponding to a given conversion rate α . The subscripts i and α represent the heating rate β of a given value and conversion (α), respectively.

$$\ln\left(\frac{\beta}{T_{\alpha,i}^2}\right) = -\frac{E_\alpha}{RT_{\alpha,i}} + \ln\left(\frac{A_\alpha R}{E_\alpha g(\alpha)}\right) \quad (12)$$

The slope was $-E_a/R$, where E_a could be obtained from a series of $\ln(\beta_i/T_{\alpha,i}^2)$ versus $1000/T_{\alpha,i}$.

2.4.4. Friedman. By introducing the heating rate into eq 6, the expression of Friedman, eq 13, can be obtained. The apparent activation energy (E_a) can be obtained at different heating rates of 10, 20, 30, 40, and 50 °C/min. A is the frequency factor (s^{-1}), with subindices i and α representing the heating rate β and conversion (α) for A given value, respectively.

$$\ln\left[\beta_i \left(\frac{d\alpha}{dT}\right)_{T_{\alpha,i}}\right] = \ln[A_\alpha f(\alpha)] - \frac{E_\alpha}{RT_{\alpha,i}} \quad (13)$$

where the slope ($-E/R$) can give the value of E_a .

2.5. Reaction Model. An important part of the kinetic analysis is the determination of the reaction model. The general method is to assume an ideal model to calculate the dynamic parameters. An accurate response model can be obtained by a master graph and regression analysis.²⁹ In general, the result obtained by the integral method differs greatly from the actual value, while the result obtained by the differential method is more accurate than that obtained by the integral method because it does not involve the approximation value in the calculation process. Equation 5 is substituted into eqs 3 and 9, and variables are separated and integrated to obtain eq 14.

$$G(\alpha) = \int_0^\alpha \frac{d\alpha}{f(\alpha)} = \frac{A}{\beta} \int_0^T \exp\left(-\frac{E}{RT}\right) dT = \left(\frac{AE}{\beta R}\right) P(u) \quad (14)$$

where $G(\alpha)$ is defined as the integral form of $f(\alpha)$; when $n = 1$, $G(\alpha) = -\ln(1 - \alpha)$; u is the integral of the temperature of $\frac{E}{RT}$ and $P(u)$; and $P(u)$ has a variety of assumptions to determine the activation energy.

The main graph method $Z(\alpha)$ is used to identify the reaction model from the ideal model set. The equation $Z(\alpha)$ can be

Table 1. Kinetic Models for Some Solid-State Reactions in Differential and Integral Forms

reaction model	coding	$f(\alpha)$	$G(\alpha)$
Avrami–Erofeev	A2	$2(1-\alpha)[- \ln(1-\alpha)]^{1/2}$	$[- \ln(1-\alpha)]^{1/2}$
1D diffusion	D1	$1/2\alpha^{-1}$	α^2
2D diffusion	D2	$[- \ln(1-\alpha)]^{-1}$	$(1-\alpha)\ln(1-\alpha) + \alpha$
Mampel (first order)	F1	$1-\alpha$	$-\ln(1-\alpha)$
second order	F2	$(1-\alpha)^2$	$(1-\alpha)^{-1} - 1$
power law	P2/3	$2/3\alpha^{-1/2}$	$\alpha^{3/2}$
power law	P2	$2\alpha^{1/2}$	$\alpha^{1/2}$
contracting cylinder	R2	$2(1-\alpha)^{1/2}$	$1 - (1-\alpha)^{1/2}$
contracting sphere	R3	$3(1-\alpha)^{2/3}$	$1 - (1-\alpha)^{1/3}$

obtained by combining the differential and integral forms of the reaction model.

$$Z(\alpha) = f(\alpha)G(\alpha) = \frac{d\alpha}{dT} T^2 \left[\frac{\pi \left(-\frac{E}{RT} \right)}{\beta T} \right] \quad (15)$$

Vasudev et al.³⁰ used some ideal dynamics models (differential and integral forms) observed in the solid-state reaction, and the primary graph method was used to change the equation of zetas $Z(\alpha)$ into a standardized equation of zetas $\frac{Z(\alpha)}{Z(0.5)}$. The term $\frac{\pi \left(-\frac{E}{RT} \right)}{\beta T}$ does not affect the shape of the functional equation. Thus, eq 13 can be written in the normalized form

$$\frac{Z(\alpha)}{Z(0.5)} = \frac{f(\alpha)G(\alpha)}{f(0.5)G(0.5)} = \left(\frac{d\alpha}{dt} \right)_{\alpha} \left(\frac{T_{\alpha}}{T_{0.5}} \right)^2 \quad (16)$$

The experimental data of $\frac{Z(\alpha)}{Z(0.5)}$ can be obtained from $\frac{d\alpha}{dt}$ and T^2 . At the same time, the reaction model³¹ (Table 1) is substituted into $f(\alpha)$ and $G(\alpha)$ to obtain the ideal simulation data graph. Then, the experimental data plots were compared with the simulated data plots to determine the kinetic characteristics of the reaction.

In addition, regression analysis was performed to obtain the dynamic model expression of the sample. Equation 10 without introducing β can be written as eq 17

$$\frac{d\alpha}{dt} = A \exp\left(-\frac{E}{RT}\right) f(\alpha) \quad (17)$$

Equation 18 is obtained by integrating eq 17

$$\ln \frac{d\alpha}{dt} = \ln[Af(\alpha)] - \frac{E}{RT} \quad (18)$$

Equation 19 is obtained by rearranging eq 17

$$f(\alpha) = \frac{d\alpha}{A dt} \exp\left(\frac{E}{RT}\right) \quad (19)$$

By rearranging to eliminate the pre-exponential factor A of the unknown value, eq 18 can be written as $H(\alpha)$ normalized equation eq 20

$$H(\alpha) = \frac{f(\alpha)}{f(0.5)} = \frac{\left(\frac{d\alpha}{dt} \right)_{\alpha}}{\left(\frac{d\alpha}{dt} \right)_{0.5}} \exp\left[\frac{E}{R} \left(\frac{1}{T_{\alpha}} - \frac{1}{T_{0.5}} \right) \right] \quad (20)$$

2.6. Mechanism Function. Figure 1 shows the function of $\frac{Z(\alpha)}{Z(0.5)}$ and the conversion rate of the α SLSx-CF-M composite

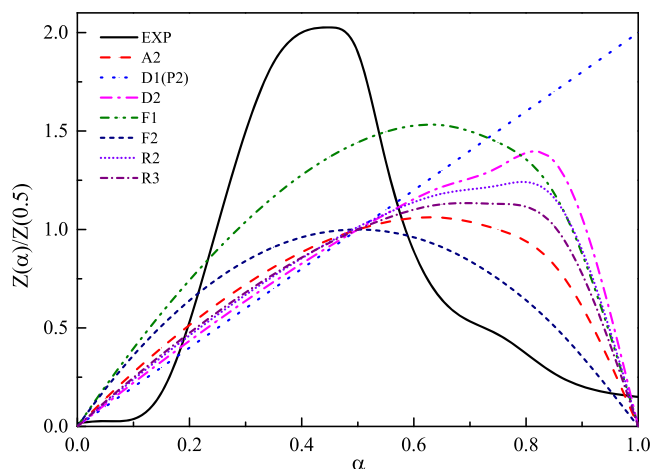


Figure 1. Diagram of different reaction models of the SLSx-CF-M composite.

film at $\beta = 30$ °C/min. By comparing and screening the experimental curve (EXP) with the curves of each reaction model, according to the reaction mechanism function proposed by Vasudev et al.,³⁰ the mechanism function used in this paper is

$$H(\alpha) = \alpha(1-\alpha)^b [-\ln(1-\alpha)]^c \quad (21)$$

Figure 2 shows the fitting curve of the SLSx-CF-M composite film mechanism function. The value of $H(\alpha)$ can be obtained by substituting the corresponding value of conversion in eq 18

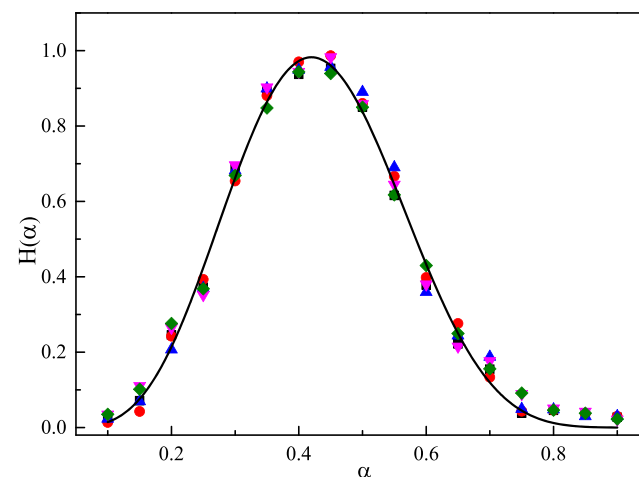


Figure 2. Diagram of the fitting curve of the mechanism function of the SLSx-CF-M composite film.

through the triglyceride test. Then, we obtain function parameter-related entities (see Table 2) by fitting.

Table 2. Parameter Values of the Mechanism Function of the SLSx-CF-M Composite Film

related parameters	<i>a</i>	<i>b</i>	<i>c</i>	<i>R</i> ²
the numerical	3277.19	9.27	5.05	0.99
the mechanism function	$H(\alpha) = 3277.19(1 - \alpha)^{9.27}[-\ln(1 - \alpha)]^{5.05}$			

2.7. Compensation Effect. The relationship between the pre-exponential factor and activation energy reflects the reaction model changes during the pyrolysis reaction.³² Figure 3 shows

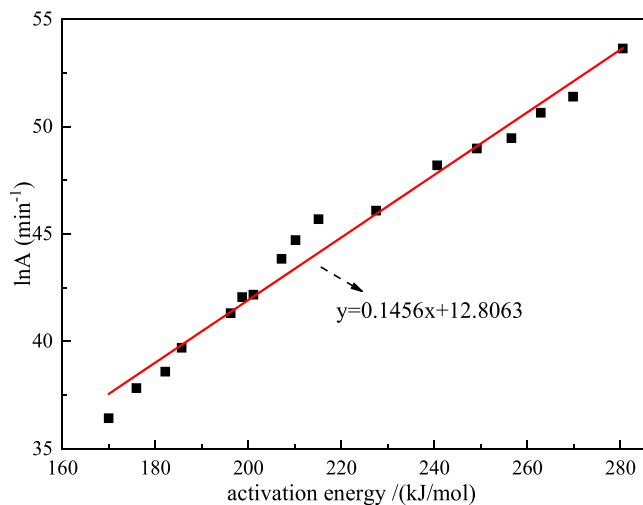


Figure 3. Correlation between activation energies and pre-exponential factors of the SLSx-CF-M composite film.

the relationship between the pre-exponential factor and activation energy corresponding to different conversion rates in the thermal decomposition process of the SLSx-CF-M composite film. As can be seen from the figure, there is a linear correlation between the pre-exponential factor and the activation energy. The fitting coefficient *R*² is 0.989, and the compensation effect is obvious with a high fitting degree.

Therefore, it can be concluded that the reaction model has no change during the whole reaction process.

3. RESULTS AND DISCUSSION

3.1. Thermogravimetric-Derivative Thermogravimetric (TG-DTG) Analysis. The thermal decomposition of the SLSx-CF-M composite film at different heating rates is a simple decomposition process. Figure 4b shows that there are two main mass-loss areas in the SLSx-CF-M composite film DTG curves at different heating rates. The first mass-loss area is located in the temperature range of 30–190 °C, mainly caused by the evaporation of water. The second weightlessness zone is in the 190–430 °C range, mainly caused by the thermal decomposition of film samples. As can be seen in the Figure 4 DTG diagram, with increasing heating rate, the maximum weight loss peaks are two weight-loss regions that migrate to higher temperatures, primarily due to the limitations of thermal mass transfer. At a higher heating rate, the sample does not have enough time to absorb heat fully. As a result, the actual temperature is lower than the reference temperature of the system, making the initial and the termination temperature of weight loss higher.³³ Taking the heating rates of 20 and 30 °C/min as examples, the initial weight-loss temperature of the SLSx-CF-M composite film in the first weight-loss stage increased from 31.6 to 32.6 °C, the maximum weight-loss temperature increased from 87.9 to 116.8 °C, and the maximum mass-loss rate of the SLSx-CF-M composite film changed from 3.40 to 3.57%/min. In the second weight-loss stage, the initial decomposition temperature increased from 264.6 to 269.4 °C, the maximum weight-loss temperature increased from 294.8 to 299.9 °C, and the maximum mass-loss rate increased from 31.43 to 53.87%/min (Table 3).

As shown in Figure 5, the curves of $\alpha-T$ and $\alpha'-T$ of the SLSx-CF-M composite film have similar variation trends under different heating rates. Figure 5a shows the relationship between conversion rate (α) and temperature (*T*) in the pyrolysis process. At 20 °C/min, the temperature range of 30–132 °C is the first stage of the rapid conversion rate growth, and the conversion rate reaches the maximum at 85 °C. In the temperature range of 132–217 °C, the conversion rate changes slowly. The 217–418 °C conversion is the second stage of rapid growth, with the maximum conversion rate at 294 °C. After 418

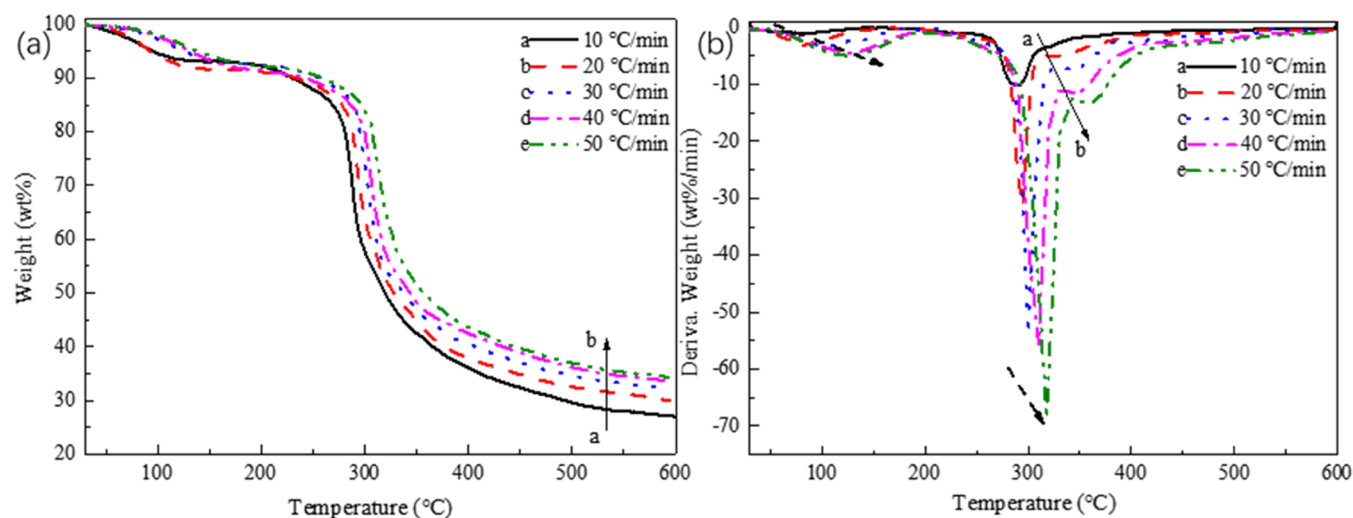
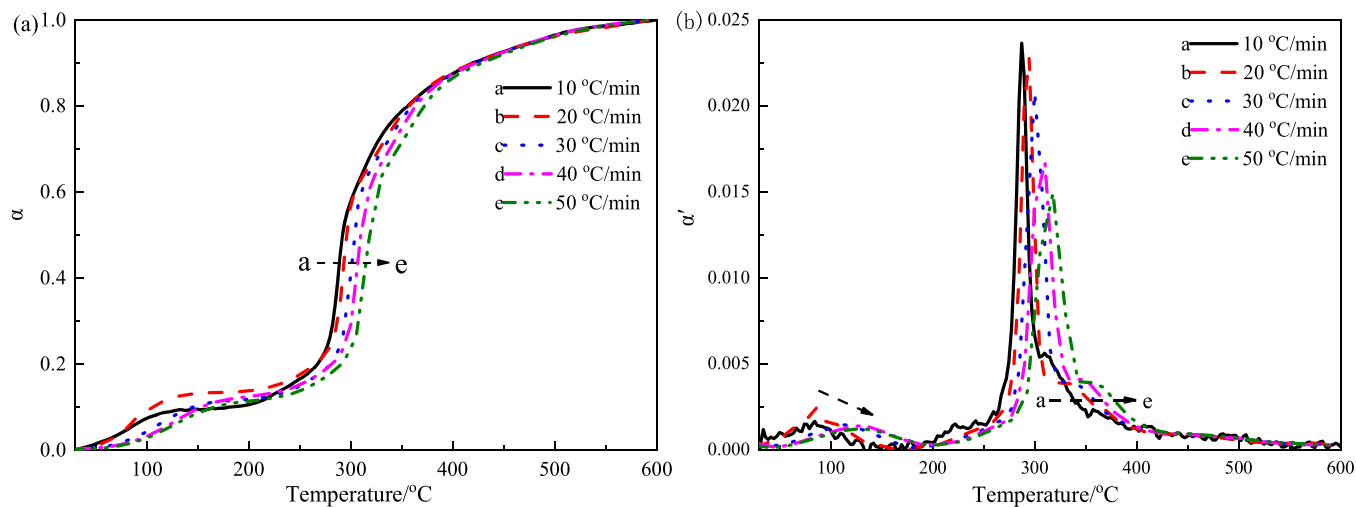


Figure 4. TG (a) and DTG (b) curves of SLSx-CF-M at different heating rates.

Table 3. TGA Date of the SLSx-CF-M Composite Film at Different Heating Rates

heating rate (°C/min)	first weightlessness stage			second weightlessness stage		
	temperature of initial decomposition (°C)	maximum weight loss temperature (°C)	maximum mass-loss rate (%/min)	temperature of initial decomposition (°C)	maximum weight loss temperature (°C)	maximum mass-loss rate (%/min)
10	30.9	84.3	1.23	258.8	289.8	10.19
20	31.6	87.9	3.40	264.6	294.8	31.43
30	32.6	116.8	3.57	269.4	299.9	53.87
40	34.3	124.1	4.45	279.4	310.2	55.68
50	35.7	134.1	4.93	281.0	318.0	68.59

Figure 5. $\alpha-T$ (a) and $\alpha'-T$ (b) curves of the SLSx-CF-M composite film at different heating rates.

°C, the increase rate of conversion tended to be flat with the increase of temperature. Figure 5b shows the relationship between the growth rate of conversion rate (α') and temperature (T) in the pyrolysis process. It can be seen from the figure that the maximum growth rate of conversion rate shifts to the right with the increase of the heating rate, which is consistent with the previous maximum mass-loss rate results.

3.2. Kinetic Analysis. 3.2.1. *KAS and FWO.* Table 4 shows the activation energy (E) and the pre-exponential factor ($\ln A$) for different conversion rates based on KAS and FWO methods. The slope determines the activation energy, and the intercept of the regression line determines the pre-exponential factor. It can be observed from the table that the pyrolysis activation energies of the SLSx-CF-M composite film are different, which indicates

that a complex multistep reaction mechanism exists in the pyrolysis process of the SLSx-CF-M composite film. Figure 6

Table 4. Activation Energy and Pre-exponential Factor Obtained by KAS and FWO Methods for the SLSx-CF-M Composite Film at Different Conversion Rates^a

α	KAS			FWO		
	E (kJ/mol)	$\ln A$ (min ⁻¹)	R^2	E (kJ/mol)	$\ln A$ (min ⁻¹)	R^2
0.05	47.34	5.27	0.995	50.91	13.81	0.996
0.15	118.75	18.31	0.991	121.28	27.55	0.992
0.25	151.56	24.60	0.999	152.93	33.93	0.999
0.35	157.04	25.86	0.994	158.24	35.17	0.995
0.45	188.90	32.67	0.991	188.63	42.04	0.992
0.55	209.19	36.93	0.993	207.99	46.30	0.993
0.65	259.20	46.54	0.986	255.75	55.95	0.987
0.75	297.28	52.46	0.995	292.29	61.94	0.995
0.85	326.64	55.78	0.991	320.63	65.35	0.991

^a R^2 is the linear correlation coefficient.

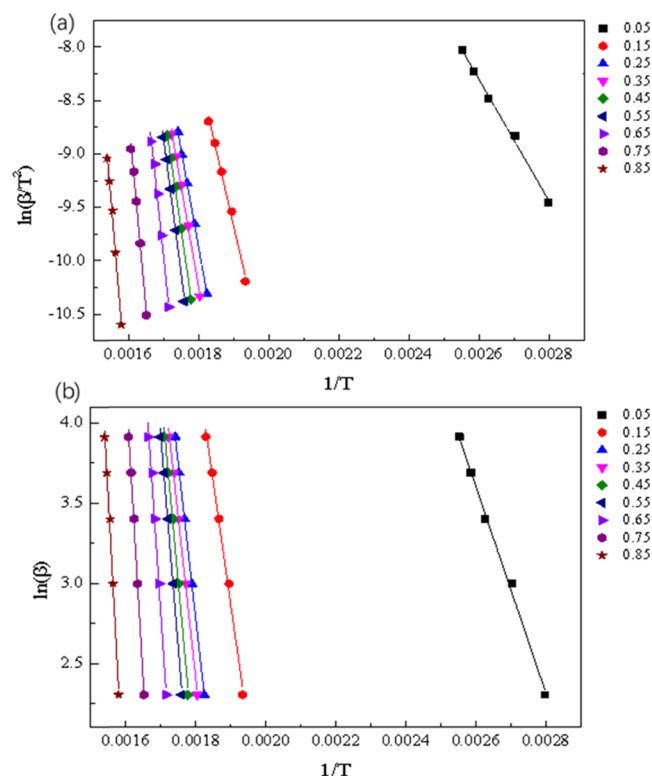


Figure 6. Linearization fitting diagram of KAS (a) and FWO (b) methods for the SLSx-CF-M composite film.

shows the linearization fitting diagram for KAS and FWO pyrolysis at a conversion rate of 0.05–0.85. The determination coefficient R^2 of the fitting line is between 0.986 and 0.999, indicating that the data is well fitted.

Figure 7 shows the activation energy variation of the SLSx-CF-M composite film obtained by the two methods under

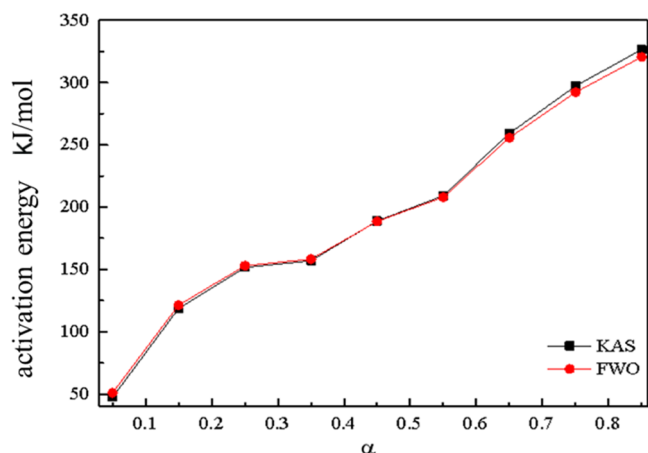


Figure 7. Changes in activation energy of the SLSx-CF-M composite film in KAS and FWO kinetic models.

different conversion rates. In addition, the activation energy trends obtained by the two methods are similar, and the data difference is slight, which indicates that the estimated values obtained are reliable. It can be seen from the figure that there are three main stages in the thermal decomposition process: the initial decomposition of the SLSx-CF-M composite film ($0.05 < \alpha < 0.25$), the middle SLSx-CF-M composite film decomposition stage ($0.25 < \alpha < 0.55$), and the late decomposition of the SLSx-CF-M composite film ($0.55 < \alpha < 0.90$).

The activation energy required for the initial decomposition ($0.05 < \alpha < 0.25$) of the SLSx-CF-M composite film is relatively less. According to the table, the activation energy required by the KAS and FWO methods for the SLSx-CF-M composite film is 47.34–118.75 and 50.91–121.28 kJ/mol, respectively. In this stage, the evaporation of water contained in the SLSx-CF-M composite film, the volatilization of eugenol, and the release of

eugenol caused by the crack of the capsule wall caused by heat are the main causes, which require low activation energy.

In the middle stage of the SLSx-CF-M composite film decomposition ($0.25 < \alpha < 0.55$), the activation energy obtained by the KAS and FWO methods was 151.56–209.19 and 152.93–207.99 kJ/mol, respectively. Among the three stages, the difference of activation energy obtained by the two methods is the smallest. The absolute difference was between 0.27 and 1.73 kJ/mol. In this stage, the random pyrolysis of the polymer in the SLSx-CF-M composite film forms an insulating carbon layer, which slows down the decomposition of the internal structural units and increases the activation energy.

The SLSx-CF-M composite film post decomposition ($0.55 < \alpha < 0.90$) of a large number of low-activity carbon-dense layers shows a rapid increase in the activation energy. According to Table 4, when the conversion rate is 0.85, the required activation energy obtained by the KAS method is 326.64 kJ/mol, which increases by 117.45 kJ/mol compared with the required activation energy at the middle and end of the term, and the required activation energy obtained by the FWO method is 320.63 kJ/mol, which increases by 112.64 kJ/mol.

3.2.2. Friedman. Figure 8a shows the result of Friedman's analysis. Table 5 shows the corresponding activation energy, pre-exponential factor, and the corresponding linear fitting determination coefficient under different conversion rates obtained based on the Friedman method. The determination coefficient R^2 of the fitting line is between 0.996 and 0.998, indicating that the data is well fitted. Figure 8b shows the change curves of activation energy E and conversion rate α during pyrolysis of the SLSx-CF-M composite film. Compared with KAS and FWO, the activation energy values obtained by the Friedman method are slightly different from those obtained by the other two methods. In $\alpha > 0.65$, the activation energy obtained by the Friedman method is smaller than that obtained by the other two methods, α is 0.85, and the difference of activation energy is 46.1–40.09 kJ/mol. However, the trend of E – α curves obtained by the three methods is roughly similar.

4. CONCLUSIONS

1. A SLSx-CF-M composite film was investigated by thermogravimetric analysis at a heating rate of 10–50 °C/min, and activation energy and pre-exponential

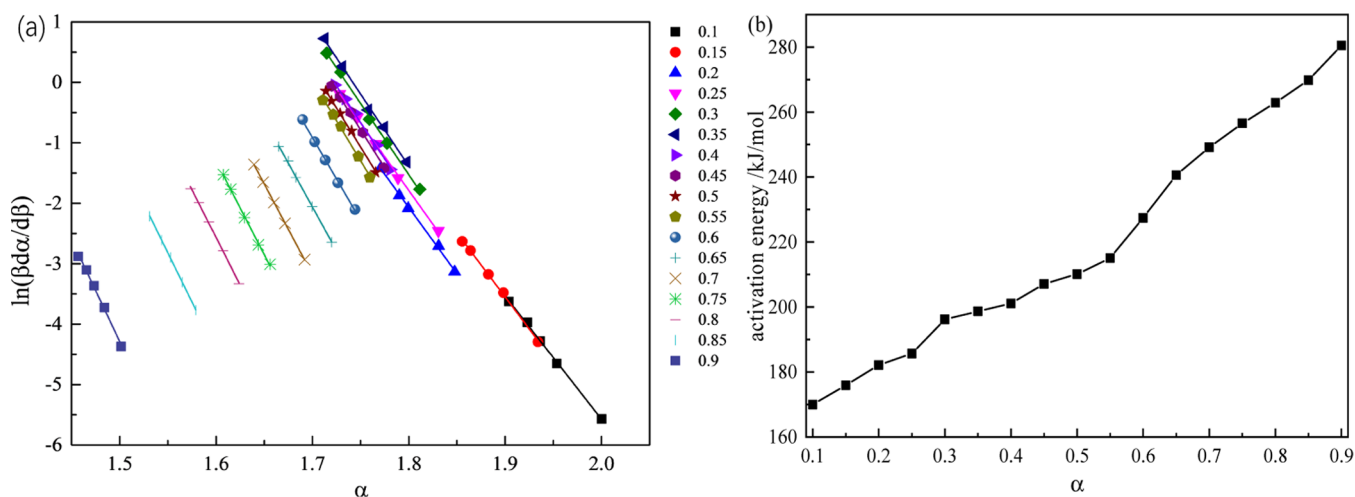


Figure 8. Friedman analysis for the pyrolysis of SLSx-CF-M composite film: linearization fitting diagram (a) and the E – α curve (b).

Table 5. Activation Energy and Pre-exponential Factor Obtained by the Friedman Method for the SLSx-CF-M Composite Film at Different Conversion Rates^a

α	E (kJ/mol)	$\ln A$ (min ⁻¹)	R^2
0.1	169.98	36.42	0.999
0.15	175.95	37.83	0.998
0.2	182.15	38.59	0.997
0.25	185.68	39.70	0.998
0.3	196.21	41.31	0.998
0.35	198.69	42.06	0.996
0.4	201.09	42.18	0.997
0.45	207.14	43.84	0.997
0.5	210.16	44.72	0.998
0.55	215.11	45.69	0.996
0.6	227.47	46.49	0.998
0.65	240.63	48.19	0.999
0.7	249.17	48.97	0.999
0.75	256.58	49.46	0.998
0.8	262.89	50.64	0.998
0.85	269.85	51.38	0.999
0.9	280.54	53.63	0.997

^a R^2 is the linear correlation coefficient.

factors during pyrolysis were calculated by KAS, FWO, and Friedman methods. The compensation effect indicates that the reaction model of the SLSx-CF-M composite film was not changed during the pyrolysis process.

- The three methods can show that the pyrolysis process can be divided into the initial volatilization ($0.05 < \alpha < 0.25$), middle organic monomer decomposition ($0.25 < \alpha < 0.55$), and the later carbon generation stages ($0.55 < \alpha < 0.95$).
- According to the changing trend of the relationship between the calculated activation energy and the conversion rate, the increase of the pyrolysis degree is positively correlated with the increased required activation energy.

AUTHOR INFORMATION

Corresponding Authors

Xinyu Lu – Co-Innovation Center for Efficient Processing and Utilization of Forest Products, College of Chemical Engineering, Nanjing Forestry University, 210037 Nanjing, China; Email: NJFULXY@outlook.com

Xiaoli Gu – Co-Innovation Center for Efficient Processing and Utilization of Forest Products, College of Chemical Engineering, Nanjing Forestry University, 210037 Nanjing, China; orcid.org/0000-0001-8588-0358; Email: guxiaoli@njfu.edu.cn

Author

Ruohan Yang – Co-Innovation Center for Efficient Processing and Utilization of Forest Products, College of Chemical Engineering, Nanjing Forestry University, 210037 Nanjing, China

Complete contact information is available at:
<https://pubs.acs.org/10.1021/acsomega.1c05289>

Author Contributions

Conceptualization, R.Y.; methodology, R.Y.; software, X.L.; validation, R.Y. and X.L.; formal analysis, R.Y.; investigation,

X.G.; resources, X.G. and X.L.; data curation, R.Y.; writing—original draft preparation, R.Y.; writing—review and editing, X.G. and X.L.; supervision, X.G.; project administration, R.Y.; and funding acquisition, X.G. All authors have read and agreed to the published version of the manuscript.

Notes

The authors declare no competing financial interest.

ACKNOWLEDGMENTS

This research was financially supported by the National Natural Science Foundation of China (no. 21774059), the Priority Academic Program Development (PAPD) of Jiangsu Higher Education Institutions, and the College Students' Practice and Innovation Training Project (202110298003Z).

REFERENCES

- Mohanty, A. K.; Misra, M.; Drzal, L. T. Surface modifications of natural fibers and performance of the resulting biocomposites: An overview. *Compos. Interfaces* **2001**, *8*, 313–343.
- Hu, D.; Wang, L. Preparation and characterization of antibacterial films based on polyvinyl alcohol/quaternized cellulose. *React. Funct. Polym.* **2016**, *101*, 90–98.
- Kong, L.; Zhang, D.; Shao, Z.; Han, B.; Lv, Y.; Gao, K.; Peng, X. Superior effect of TEMPO-oxidized cellulose nanofibrils (TOCNs) on the performance of cellulose triacetate (CTA) ultrafiltration membrane. *Desalination* **2014**, *332*, 117–125.
- Lv, Y.; Du, Y.; Chen, Z.-X.; Qiu, W.-Z.; Xu, Z.-K. Nanocomposite membranes of polydopamine/electropositive nanoparticles/polyethyleneimine for nanofiltration. *J. Membr. Sci.* **2018**, *545*, 99–106.
- Puspasari, T.; Huang, T.; Sutisna, B.; Peinemann, K.-V. Cellulose-polyethyleneimine blend membranes with anomalous nanofiltration performance. *J. Membr. Sci.* **2018**, *564*, 97–105.
- Wang, Y.; Wang, C.; Xie, Y.; Yang, Y.; Zheng, Y.; Meng, H.; He, W.; Qiao, K. Highly transparent, highly flexible composite membrane with multiple antimicrobial effects used for promoting wound healing. *Carbohydr. Polym.* **2019**, *222*, No. 114985.
- Wen, Y.; Yuan, Z.; Liu, X.; Qu, J.; Yang, S.; Wang, A.; Wang, C.; Wei, B.; Xu, J.; Ni, Y. Preparation and Characterization of Lignin-Containing Cellulose Nanofibril from Poplar High-Yield Pulp via TEMPO-Mediated Oxidation and Homogenization. *ACS Sustainable Chem. Eng.* **2019**, *7*, 6131–6139.
- Qi, Y.; Lin, S.; Lan, J.; Zhan, Y.; Guo, J.; Shang, J. Fabrication of super -high transparent cellulose films with multifunctional performances via postmodification strategy. *Carbohydr. Polym.* **2021**, *260*, No. 117760.
- Wan, J.; Diao, H.; Yu, J.; Song, G.; Zhang, J. A biaxially stretched cellulose film prepared from ionic liquid solution. *Carbohydr. Polym.* **2021**, *260*, No. 117816.
- Nascimento, E. S.; Barros, M. O.; Cerqueira, M. A.; Lima, H. L.; Borges, M. dF.; Pastrana, L. M.; Gama, F. M.; Rosa, M. F.; Azeredo, H. M. C.; Gonçalves, C. All-cellulose nanocomposite films based on bacterial cellulose nanofibrils and nanocrystals. *Food Packag. Shelf Life* **2021**, *29*, No. 100715.
- Kim, H.-J.; Roy, S.; Rhim, J.-W. Effects of various types of cellulose nanofibers on the physical properties of the CNF-based films. *J. Environ. Chem. Eng.* **2021**, *9*, No. 106043.
- Carvajal, J. C.; Gomez, A.; Cardona, C. A. Comparison of lignin extraction processes: Economic and environmental assessment. *Bioresour. Technol.* **2016**, *214*, 468–476.
- Demuner, I. F.; Borges Gomes, F. J.; Gomes, J. S.; Coura, M. R.; Borges, F. P.; Macedo Ladeira Carvalho, A. M.; Silva, C. M. Improving kraft pulp mill sustainability by lignosulfonates production from processes residues. *J. Cleaner Prod.* **2021**, *317*, No. 128286.
- Wu, R.-L.; Wang, X.-L.; Li, F.; Li, H.-Z.; Wang, Y.-Z. Green composite films prepared from cellulose, starch and lignin in room-temperature ionic liquid. *Bioresour. Technol.* **2009**, *100*, 2569–2574.

- (15) Zhang, C. W.; Nair, S. S.; Chen, H.; Yan, N.; Farnood, R.; Li, F. Y. Thermally stable, enhanced water barrier, high strength starch bio-composite reinforced with lignin containing cellulose nanofibrils. *Carbohydr. Polym.* **2020**, *230*, No. 115626.
- (16) Michelin, M.; Marques, A. M.; Pastrana, L. M.; Teixeira, J. A.; Cerqueira, M. A. Carboxymethyl cellulose-based films: Effect of organosolv lignin incorporation on physicochemical and antioxidant properties. *J. Food Eng.* **2020**, *285*, No. 110107.
- (17) Feng, S.; Shui, T.; Wang, H.; Ai, X.; Kuboki, T.; Xu, C. C. Properties of phenolic adhesives formulated with activated organosolv lignin derived from cornstalk. *Ind. Crops Prod.* **2021**, *161*, No. 113225.
- (18) Lamaming, J.; Heng, N. B.; Owodunni, A. A.; Lamaming, S. Z.; Abd Khadir, N. K.; Hashim, R.; Sulaiman, O.; Kassim, M. H. M.; Hussin, M. H.; Bustami, Y.; Amini, M. H. M.; Hiziroglu, S. Characterization of rubberwood particleboard made using carboxymethyl starch mixed with polyvinyl alcohol as adhesive. *Composites, Part B* **2020**, *183*, No. 107731.
- (19) Yin, H.; Zheng, P.; Zhang, E.; Rao, J.; Lin, Q.; Fan, M.; Zhu, Z.; Zeng, Q.; Chen, N. Improved wet shear strength in eco-friendly starch-cellulosic adhesives for woody composites. *Carbohydr. Polym.* **2020**, *250*, No. 116884.
- (20) Bao, L.; Zhang, F.; Chen, T.; Cao, J.; Chen, Y.; Bai, Y. Novel submicron poly(urea-formaldehyde) and essence of jasmine microcapsules with enhanced sustained release. *Flavour Fragrance J.* **2015**, *30*, 459–466.
- (21) Yan, L.; Zeng, F.; Chen, Z.; Chen, S.; Lei, Y. Improvement of wood decay resistance by salicylic acid / silica microcapsule: Effects on the salicylic leaching, microscopic structure and decay resistance. *Int. Biodeterior. Biodegrad.* **2021**, *156*, No. 105134.
- (22) Nguon, O.; Lagugne-Labarthe, F.; Brandys, F. A.; Li, J.; Gillies, E. R. Microencapsulation by in situ Polymerization of Amino Resins. *Polym. Rev.* **2018**, *58*, 326–375.
- (23) Zhang, Y.; Rochefort, D. Characterisation and applications of microcapsules obtained by interfacial polycondensation. *J. Microencapsulation* **2012**, *29*, 636–649.
- (24) Fu, F.; Li, L.; Liu, L.; Cai, J.; Zhang, Y.; Zhou, J.; Zhang, L. Construction of Cellulose Based ZnO Nanocomposite Films with Antibacterial Properties through One-Step Coagulation. *ACS Appl. Mater. Interfaces* **2015**, *7*, 2597–2606.
- (25) Guo, Y.; Zhou, J.; Song, Y.; Zhang, L. An Efficient and Environmentally Friendly Method for the Synthesis of Cellulose Carbamate by Microwave Heating. *Macromol. Rapid Commun.* **2009**, *30*, 1504–1508.
- (26) Li, W.; Li, T.; Li, G.; An, L.; Li, F.; Zhang, Z. Electrospun H₄SiW₁₂O₄₀/cellulose acetate composite nanofibrous membrane for photocatalytic degradation of tetracycline and methyl orange with different mechanism. *Carbohydr. Polym.* **2017**, *168*, 153–162.
- (27) Qi, H.; Liebert, T.; Meister, F.; Zhang, L.; Heinze, T. Homogenous Carboxymethylation of Cellulose in the New Alkaline Solvent LiOH/Urea Aqueous Solution. *Macromol. Symp.* **2010**, *294*, 125–132.
- (28) He, Z.; Jiang, S.; Li, Q.; Wang, J.; Zhao, Y.; Kang, M. Facile and cost-effective synthesis of isocyanate microcapsules via polyvinyl alcohol-mediated interfacial polymerization and their application in self-healing materials. *Compos. Sci. Technol.* **2017**, *138*, 15–23.
- (29) Várhegyi, G.; Wang, L.; Skreiberg, O. Towards a meaningful non-isothermal kinetics for biomass materials and other complex organic samples. *J. Therm. Anal. Calorim.* **2018**, *133*, 703–712.
- (30) Vasudev, V.; Ku, X.; Lin, J. Kinetic study and pyrolysis characteristics of algal and lignocellulosic biomasses. *Bioresour. Technol.* **2019**, *288*, No. 121496.
- (31) Hu, M.; Chen, Z.; Guo, D.; Liu, C.; Xiao, B.; Hu, Z.; Liu, S. Thermogravimetric study on pyrolysis kinetics of *Chlorella pyrenoidosa* and bloom-forming cyanobacteria. *Bioresour. Technol.* **2015**, *177*, 41–50.
- (32) Brems, A.; Baeyens, J.; Beerlandt, J.; Dewil, R. Thermogravimetric pyrolysis of waste polyethylene-terephthalate and polystyrene: A critical assessment of kinetics modelling. *Resour., Conserv. Recycl.* **2011**, *55*, 772–781.
- (33) Ma, Z.; Chen, D.; Gu, J.; Bao, B.; Zhang, Q. Determination of pyrolysis characteristics and kinetics of palm kernel shell using TGA-FTIR and model-free integral methods. *Energy Convers. Manage.* **2015**, *89*, 251–259.